



**HAL**  
open science

## Understanding and overcoming proximity effects in multi-spot two-photon direct laser writing

Caroline Arnoux, Luis Pérez-Covarrubias, Alexandre Khaldi, Quentin Carlier,  
Patrice Baldeck, Kevin Heggarty, Akos Banyasz, Cyrille Monnereau

► **To cite this version:**

Caroline Arnoux, Luis Pérez-Covarrubias, Alexandre Khaldi, Quentin Carlier, Patrice Baldeck, et al.. Understanding and overcoming proximity effects in multi-spot two-photon direct laser writing. Additive Manufacturing, 2022, 49, pp.102491. 10.1016/j.addma.2021.102491 . hal-03590641

**HAL Id: hal-03590641**

**<https://hal.science/hal-03590641>**

Submitted on 4 Mar 2022

**HAL** is a multi-disciplinary open access archive for the deposit and dissemination of scientific research documents, whether they are published or not. The documents may come from teaching and research institutions in France or abroad, or from public or private research centers.

L'archive ouverte pluridisciplinaire **HAL**, est destinée au dépôt et à la diffusion de documents scientifiques de niveau recherche, publiés ou non, émanant des établissements d'enseignement et de recherche français ou étrangers, des laboratoires publics ou privés.

1

2 **FRONT MATTER**

3

4 **Understanding and Overcoming Proximity Effects in Multi-Spot Two-Photon Direct Laser**  
5 **Writing**

6

7 **Authors**

8

Caroline Arnoux,<sup>1\*</sup> Luis A. Pérez-Covarrubias,<sup>2</sup> Alexandre Khaldi,<sup>2</sup> Quentin Carlier,<sup>2</sup>  
9 Patrice L. Baldeck,<sup>1</sup> Kevin Heggarty,<sup>2\*</sup> Akos Banyasz<sup>1</sup> and Cyrille Monnereau<sup>1</sup>

10

11 **Affiliations**

12

<sup>1</sup> Univ. Lyon, ENS Lyon, CNRS, Université Lyon 1, Laboratoire de Chimie, UMR 5182,  
13 46 Allée d'Italie, 69364 Lyon, France.

14

<sup>2</sup> IMT-Atlantique, Optics Department, Technopole Brest-Iroise, 29285, BREST, France.

15

16 c.caroline.arnoux@gmail.com

17 kevin.heggarty@imt-atlantique.fr

18

19 **Abstract**

20

Although additive manufacturing using multi-photon direct laser writing is nowadays  
21 considered as a major tool in the fabrication of future nano/micro-objects and optical  
22 components, it is currently limited by the low throughput of the writing process. To  
23 circumvent this issue, massive parallelization of the write process is a very promising  
24 avenue. However, simultaneous writing of structures in close spatial proximity generates  
25 fabrication artefacts, collectively referred to as “proximity effects”, which strongly limit the  
26 accessible structure resolution. In this work, we systematically investigate the experimental  
27 parameters that influence these effects using specifically designed  $N \times N$  spot diffractive  
28 optical elements. Through computer simulations, we show that these effects can be modeled  
29 remarkably successfully simply by taking Point Spread Function overlap and diffusion  
30 processes into account. We illustrate the usefulness of the concept by designing a parallel  
31 write approach giving access to periodic structures with short inter-object distances while  
32 very largely overcoming proximity effects.

33

34 **Teaser**

35

Combining experience and modeling, we identify the physicochemical origin of proximity  
36 effects in parallel microfabrication.

37

38 **MAIN TEXT**

39

40 **Introduction**

41

Additive manufacturing has attracted increasing interest due to the large number of  
42 applications that can be addressed, from aeronautics to medical devices and optics (1). Large  
43 surfaces with micron and sub-micron patterns such as lens arrays for sensors or micro-  
44 needle arrays for drug delivery are part of the structures that can be built by two-photon  
45

46 induced polymerization (TPP) also called direct laser writing (DLW) (1–3). Through  
47 focusing a laser source into a small volume of liquid resin with a high numerical aperture  
48 objective, this technique enables the fabrication of complex and highly-resolved three-  
49 dimensional (3D) microstructures.

50 However, this technique suffers from long plot times for large samples (up to days for  
51 objects with dimensions in the millimeter range), which currently slows down its entry into  
52 the industrial applications market (1–3). To overcome this major limitation, different  
53 strategies have been implemented such as the use of galvanometer scanners to increase the  
54 scanning speed, whether or not in association with multi-focus spot setups. Multi-foci can  
55 be provided by microlens arrays (MLA), spatial light modulators (SLM), ultrafast random-  
56 access digital micromirror devices (DMD) or diffractive optical elements (DOE) (4–13). In  
57 all these strategies, massive parallelization increases throughput by increasing the number  
58 of focal spots used simultaneously so that large areas or arrays of periodic structures can be  
59 written in the same time frame traditionally used to fabricate a single structure with a single  
60 beam.

61 Unfortunately, this parallelization can have a detrimental effect on the uniformity of the  
62 repeated structures due to the so-called “proximity effects”. Polymerization appears to  
63 depend on the local photochemical environment and the intensity distribution further away  
64 from the desired focal spots. Thus, reducing the distance between structures proves to be  
65 more challenging than reducing the feature sizes due to structure broadening (14–16) and  
66 sporadic connections (15, 17–19) that arise between them. When simultaneously exposing  
67 several spots, this effect is exacerbated and different local TPP thresholds are observed, for  
68 example, at the center and in the corner of a write spot array. This effect is attributed to  
69 diffusion phenomena (15, 16, 20, 21) and has already been observed for conventional single  
70 photon polymerization (22) as well as in DLW, both with low one-photon absorption  
71 (LOPA) (23) and two-photon absorption (15, 16). It has even been already taken advantage  
72 of to improve surface smoothness (24). Although it has occasionally been highlighted in  
73 articles dealing with DLW, proposing tracks to correct it mainly with dynamic irradiation  
74 power control (15, 16, 22, 23, 25–27), its precise and quantitative characterization is scarce  
75 and has, to our knowledge, never been reported in detail for parallel plotting. It has also  
76 recently been identified as a key difficulty that must be overcome to enable significant  
77 parallelization speed improvements through the use of large numbers of closely spaced write  
78 spots (13).

79 In this paper, we introduce an experimental study to characterize the dependence of the  
80 proximity effects encountered in parallel microfabrication based on the use of DOEs in  
81 various experimental conditions. By proximity effects we more precisely mean: any local  
82 changes in the 2PP threshold linked to the presence of other light spots in the vicinity of a  
83 studied light spot (spatial proximity effects) or to any previous exposure of the resist -  
84 whether leading to polymerization or not - by spots scanned across the same plot area  
85 (temporal proximity effects). This approach has been combined with a phenomenological  
86 computer model allowing us to demonstrate the effect of point spread function (PSF)  
87 overlap and diffusion processes, partially quantifying the range of the effect under specific  
88 conditions. We thus highlight three distinct regimes depending on the write spot separation:  
89 i/ small inter-structure spacings where light spot overlap effects outside the focal plane  
90 (Talbot-like effects) make any attempt of parallel two-photon DLW extremely challenging;  
91 ii/ intermediate spacings in which diffusion (for example of radicals) plays an important  
92 role in creating “crosstalk” between exposed spots (proximity effects) and undesired over-  
93 polymerization that can, however, be overcome; iii/ large spacings where no particular

difficulties arise. Ultimately, we show that it is possible to circumvent these proximity effects using larger separations between spots.

This work provides a better understanding of the role of diffusion in proximity effects, and offers new insights for massively parallelized two-photon DLW generally considered today to be one of the most promising approaches for high-throughput, high-resolution manufacturing (13).

## Results

### A qualitative illustration of proximity effects in parallel write

An introductory illustration of the proximity effects can be seen in **Fig. 1**, where one of the resists involved in the study (PR\_hybrid Ormocomp/V-Shape, see experimental section for details about the composition) is exposed with an array of irradiation beams ( $5 \times 5$  spot array with a  $2.22 \mu\text{m}$  inter-spot distance) of increasing irradiation intensity. At low intensity, all irradiated spots present a similar polymerization pattern, slight variations being due to non-uniformities in the diffraction pattern resulting from imperfections in DOE fabrication (see experimental section). Upon increasing the intensity, it becomes very apparent that the pattern progressively changes, with an increased polymerization efficiency in the center in comparison with the periphery (**Fig. 1**). This evolution corresponds to increasing overlap and crosstalk in the exposed area, and can be influenced by many parameters that we will explore in the rest of this article.

(Insert Figure 1)

### Influence of the write spot separation

**Fig. 2A** features two structures fabricated with spot arrays with an equal number of spots but different spot separations. The observed differences clearly illustrate the influence of the spot separation: small spacing increases the inhomogeneity even with short exposure times. Thus, it is not possible to achieve homogeneous polymerization of each voxel structure using an  $11 \times 11$  spot DOE with an inter-spot distance of  $0.62 \mu\text{m}$  whereas the analogue structure is easily obtained with an  $11 \times 11$  spot DOE with a three times greater inter-spot distance ( $1.85 \mu\text{m}$ ). Note that the array of voxel structures with the  $0.62 \mu\text{m}$  spacing observed in **Fig. 2A**, was obtained with hundred-times shorter exposure time compared to that used for the fabrication with the  $1.85 \mu\text{m}$  spaced DOE. The central overpolymerization observed with the closely spaced spots is accompanied by an underpolymerization of the peripheral structures, so that some of the voxel structures in the last two rows were washed away during the development step. This behaviour supports the hypothesis that the proximity of the spots during simultaneous exposure contributes to reducing the overall polymerization threshold of each structure written in parallel, all the more so as we move closer to the center of the structure array. At small write spot spacings, this results in a non-uniform spatial profile of the polymerization threshold and a decrease of each threshold compared to sequential single-beam writing (27, 28).

(Insert Figure 2)

138 In order to test this hypothesis, we modelled these experimental conditions in our digital  
139 simulations by using 585 and 58500 laser pulses to take into account the experimental  
140 exposure times (50 ms and 5 s, respectively) and laser repetition rate (11.7 kHz). **Fig. 2B**  
141 shows the results of these simulations for the 100× NA 1.40 objective PSF with write spot  
142 spacings of 0.6 μm (left) and 1.8 μm (right), the approximation in the choice of the  
143 simulated distances being imposed by the characteristics of our sampling grid (see  
144 experimental section).

145 We first simulated the overlapping of the PSFs without introducing diffusion effects into  
146 the numerical model (Fig. S1). In this case, no overpolymerized areas were observed in the  
147 simulated structures. In contrast, when adding diffusion and decay parameters in the  
148 simulations, an overall result that is remarkably similar to the experimentally obtained  
149 structures was achieved (**Fig. 2B**). Despite our digital model's simplicity, this result  
150 indicates that the simulation of the parallel write process as a PSF overlap and basic  
151 diffusion process appears to be a reasonably accurate description.

### (Insert Figure 3)

155 The influence of inter-spot separation in the polymerization threshold is even more clearly  
156 demonstrated in **Fig. 3** showing microfabricated voxel structure arrays obtained with  
157 different spacings but in otherwise identical exposure conditions.

159 While reducing the inter-spot distance from *ca.* 5.6 μm to 2.2 μm, the voxel array remains  
160 reasonably homogeneous, except for the slightly over-corrected central spot; indeed, the  
161 array is more uniform, indicating a possible use of the proximity effects as a corrective  
162 parameter to the overcorrection of zero-order. However, at a 0.9 μm inter-spot distance, the  
163 voxel structures at the edges appear clearly smaller than those that are closer to the center  
164 and uncontrolled polymerization has occurred at the center, resulting in structures with ill-  
165 controlled height and the merging of individual voxels into an undefined intricate structure.  
166 Again, the experimental results were confronted with numerical simulations using the same  
167 model as described above. The results of the corresponding simulations in which 5×5 spot  
168 arrays with different separations (5.6 μm, 2.2 μm and 0.8 μm) were used, can be seen in  
169 **Fig. 4**. Based on the exposure time and laser repetition rate, 585 laser pulses were considered  
170 in each case and the diffusion parameters were kept constant compared to the previous  
171 simulation since the experiments were conducted with the same resin (see Table S1). A  
172 decay factor of 0.995 (assuming exponential decay) corresponds to a species half-life of  
173 0.012 s, in good agreement with previously reported values for short-lived radical species  
174 (29). As in the previous experiment, we can see a strong similarity between the simulated  
175 structures and the experimental results. A noticeable difference is the height of the simulated  
176 structures which tends to saturate (“flat top”) as a consequence of the limited Z range of the  
177 simulations (computing load limitations).

### (Insert Figure 4)

181 In the experiments at small inter-spot distances, these typical overpolymerized structures,  
182 which seem to spread vertically above the focal plane, could result from “out-of-plane”  
183 overlap of the PSFs. As the light focused by the microscope objective converges to form  
184 the array of spots in the focal plane, the local light energy density increases towards the  
185 write spot locations. If the spots in the array are sufficiently separated, the energy density  
186 will be too low outside the focal plane for overlap between the light fields from the different  
187 light spots to reach the polymerization threshold. However, when the spots are closer

188 together, at planes close to the focal plane, the converging light may concentrate sufficiently  
189 for overlap to produce polymerization (see Fig. S2).

190 This generation of out of focus plane “hot spots” bears some resemblance to the well-known  
191 Talbot effect which can lead to periodic repetitions of an image of the spot pattern at regular  
192 distances away from the focal plane, the first layer being shifted by half the period of the  
193 focal spot pattern (30). The Talbot effect has already been used for patterning and 3D  
194 printing applications such as displacement Talbot lithography (31, 32) or proximity field  
195 nanopatterning (33). However, the Talbot effect generally occurs when all the spots in a  
196 regular array have the same light field phase. This is not the case with the DOEs used here  
197 since they generate spots with random light field phases and are therefore likely to produce  
198 random interference patterns due to overlap in out of focus planes.

199 Such effects are also clearly seen in Fig. S3, showing structures obtained when using a small  
200 spot separation write-spot array that was scanned to write “L” shaped motifs: increasing the  
201 incident light power results in the progressive formation of a multi-layered periodic  
202 structure along the Z axis. Although clearly distinct from the diffusion-related proximity  
203 effect illustrated in the previous and following examples, it also results in undesired  
204 polymerization peaking at the center of the generated motif, and should be taken into  
205 account in parallel fabrication especially when generating periodic structures with short  
206 inter-voxel distances.

### 207 **Influence of the Objective Numerical Aperture**

208 Besides inter-spot distance which partly depends on the magnification of the objective, the  
209 numerical aperture of the objective used for the fabrication is another important parameter  
210 that influences proximity effects, because it will affect light distribution and inter-spot  
211 overlaps of the PSF functions. In order to address this issue, parallel fabrication using a 0.95  
212 NA (Zeiss 40× Apochromat) and a 1.40 NA (Zeiss 100× Apochromat) microscope objective  
213 were compared.

214 Due to the different magnification of the objectives, the spot spacing obtained with the 40×  
215 objective is 2.5-times that obtained with the 100× objective for the same DOE. To enable  
216 reliable comparison of both objectives at same inter spot distance in the final fabricated  
217 array of structures, we used two distinct DOEs with different output diffraction angles (DOE  
218 spatial periods) as explained in the experimental section.

219 In such conditions, **Fig. 5** establishes the superiority of the 100× objective, with the highest  
220 NA, in view of minimizing proximity effects at a given spot separation. Here the temporal  
221 component of the proximity effect is also clearly shown with the 40× objective: the height  
222 of each “L” manufactured with this objective is not constant but increases continuously  
223 during the manufacturing process (the “L” motifs being fabricated from top left to bottom  
224 right as indicated by a red arrow). The beginning of the L structure is not visible, while its  
225 end shows clear signs of over-polymerization. This indicates that as manufacturing  
226 progresses, the resin locally becomes artificially more sensitive due to prolonged exposure  
227 to the laser beams, consistent with our working-hypothesis of a time-dependant diffusion  
228 phenomenon of the generated radicals. In the present case, this effect combines with the  
229 overlapping of the light beams, strongly conditioned by the nature of the objective. A slight  
230 temporal proximity effect can still be noticed with the 100× objective, but in a more  
231 moderate way given the greater NA resulting in a better confinement of the laser intensity  
232 along the Z axis. As a consequence, it was possible to find a set of parameters leading to  
233 globally uniform structures: each individual L-shaped structure shows a relatively  
234 homogeneous width and height along the fabrication path.

**(Insert Figure 5)**

This process was simulated digitally, translating the 5×5 PSF write spot array between each laser pulse to model the laser beam scanning with arrays of two different PSF to represent the 100× NA 1.40 (**Fig. 6A**) and the 40× NA 0.95 (**Fig. 6B**) objectives. A satisfactory agreement with the experimentally observed structures was again obtained, limited to some extent by the coarse simulation grid (200 nm) imposed by the heavy simulation load. We simulated with a number of pulses corresponding to 200 nm steps at the considered scan rate (2.4  $\mu\text{m}\cdot\text{s}^{-1}$  here), meaning about 975 pulses per sampling grid position. As before, the simulated diffusion kernel  $\sigma$  value and the decay factor were adapted empirically to fit the simulations to the experimentally observed structures. This resulted in the parameters shown in Table S1 indicating a stronger diffusion behaviour in the PR\_hybrid resist. A decay factor of 0.99999 gave the best fit, corresponding to a diffusing species half-life of 5.9 s, which seems again in good agreement with previously reported values for radical species, although this lifetime is longer than that calculated in PR\_organic for reasons that will be discussed later.

**(Insert Figure 6)**

Calculations hence confirm that stronger focusing of the light results in a reduced overlap of the high intensity part of the light beams with the higher NA objective for a given inter-spot distance. As expected, the use of higher NA objectives helps to reduce the spatial extent of the PSF, making this technique a way to minimize overlap and thus reduce specific proximity effects in parallel TPP. Interestingly, in the case of these L-shaped structures, the simulations seem to reproduce not only the spatial component (decreased polymerization threshold from the periphery to the center) but also the temporal component (decreasing polymerization threshold with increasing manufacturing time as indicated by the larger and higher structures written towards the end of the plot) of the proximity effect, thereby confirming the probably crucial role of species diffusion in the overall process.

**Influence of the photoresist composition**

The spatial resolution of a photopolymerization reaction is not only influenced by the dimensions of the irradiated voxels, but ultimately also by how far growing radicals species can diffuse away from the irradiated area. The latter parameter can be influenced by multiple factors, such as radical intrinsic mobility and the presence and diffusion ability of radical quenchers, such as for instance molecular oxygen or polymerization inhibitors. Both processes are strongly dependent on the nature and composition of the photoresist.

A huge impact of the photoresist composition was indeed highlighted by the comparison between an organic resin PR\_organic based on a mixture of acrylates (DPPHA and DDA) and a hybrid resin PR\_hybrid based on a modified Ormocomp® resist. The same photoinitiator (PI) was used in both resins so that the difference lies in the monomer mixture composition (organic acrylate mixture stabilized with MEHQ on the one hand, unstabilized hybrid resin on the other). As illustrated in **Fig. 7**, the PR\_hybrid is much more reactive than the PR\_organic. Thus, fabrication of a development-resistant structure can be achieved with shorter exposure times in the PR\_hybrid resist. However, with the unstabilized PR\_hybrid resist, it was impossible to control the polymerization features in order to obtain an homogeneous periodic structure: a marked difference was systematically seen when comparing the central and the peripheral spots, with a clear overpolymerization in the center

285 compared to the corners, regardless of the fabricated test structure (1D: single voxel; 2D:  
286 L-shape; 3D: cones).

287 Conversely, it was possible to find suitable manufacturing parameters to fabricate a  
288 homogeneous network of the three selected test structures with the PR\_organic resin (a  
289 single voxel, an “L” shape with a side length of 2  $\mu\text{m}$  and a cone with a height of 1.40  $\mu\text{m}$ )  
290 at an inter-spot distance as small as 1.85  $\mu\text{m}$ .

291  
292 **(Insert Figure 7)**  
293

294 **Fig. 8** shows the corresponding simulation results. Good empirical fits to the experimental  
295 voxel structures (illustrations A and D in **Fig. 7** and **Fig. 8**) were obtained using the  
296 appropriate number of laser pulses, 58500 and 585 laser pulses for PR\_organic and  
297 PR\_hybrid respectively, and the simulation parameters used previously for both resists (see  
298 Table S1).

299 In the case of the “L” shapes simulations (illustrations B and E in **Fig. 7** and **Fig. 8**), the  
300 same diffusion parameters gave the best experimental fit, considering 19500 and 59 pulses  
301 per sample grid position every 200 nm for PR\_organic and PR\_hybrid respectively, in  
302 accordance with the scan speed.

303 These results seem to indicate that diffusion in the PR\_hybrid resist is significantly stronger  
304 than in the PR\_organic resist, being of both longer range (higher  $\sigma$  value) and with a longer  
305 diffusing species lifetime (lower decay rate). Besides, **Fig. 8B** shows significant out of focal  
306 plane polymerization which also appears in the simulations but to a more limited extent,  
307 probably because the simulations only model interactions close to the focus plane and do  
308 not take out of plane light energy into effect (computational load limitations currently  
309 prevent this). As explained above (**Fig. 4** and **Fig. S3**), such out of focus plane interactions  
310 very probably do occur (particularly for large arrays such as the  $11 \times 11$  spot array used here)  
311 and are likely to be at least partially responsible for the increased height of the experimental  
312 structures of the PR\_hybrid structures.

313 Because of the unstabilized nature of PR\_hybrid and the wide range of evidence obtained  
314 in all of the above-described experiments for the involvement of diffusion (probably of  
315 radical species) in the proximity effects and most notably the much increased lifetime of the  
316 diffusing species in PR-hybrid resist compared to PR\_organic, we hypothesized that  
317 addition of 4-methoxyphenol (MEHQ) as stabilizer should help in reducing proximity  
318 effects in the latter. Thus, a stabilized equivalent of PR\_hybrid, where 700 ppm MEHQ  
319 were added to the formulation was prepared and used for parallel microfabrication with an  
320  $11 \times 11$  spot DOE at 1.85  $\mu\text{m}$  inter-spot distance. Systematic comparison between results  
321 obtained with PR\_hybrid and PR\_hybrid stabilized with 700 ppm MEHQ (**Fig. S4**) clearly  
322 establishes that the addition of the stabilizer consistently reduces proximity effects (at the  
323 expense of reduced photoresist sensitivity). As a consequence, the quality of periodic arrays  
324 fabricated with PR\_hybrid with 700 ppm MEHQ becomes relatively similar to that obtained  
325 with PR\_organic, although a slight central over-polymerization was still observed.

326  
327 **(Insert Figure 8)**  
328

## 329 **Overcoming proximity effects**

330  
331



379 experimental parameters that determine the outcome of parallel two-photon DLW printing  
380 in our mechanistic study.

381 These data illustrate that, when parallelizing two-photon DLW using DOEs, many criteria  
382 have to be taken into account to ensure maximal efficiency of the fabrication process and  
383 fidelity in the reproduction of the pattern array.

384 In particular, we have shown that laser power, the NA of the objective, the chemical nature  
385 of the resin and, most importantly, the inter-spot distance of the projected motifs are  
386 particularly determining factors that have a strong influence on the strength of these  
387 proximity effects. Attempts to model these effects through digital simulations revealed a  
388 predominant influence of diffusion processes on the characteristics of the intensity of these  
389 proximity effects. More precisely, the characteristic diffusion length and time dependence  
390 of the diffusion phenomenon led us to formulate the hypothesis of short lived radicals being  
391 the diffusing species. As a support to this hypothesis, we showed that the introduction of  
392 ppm amounts of a free radical inhibitor (MEHQ) into the hybridOrmocomp photoresist, in  
393 which proximity effects were particularly strong, led to a marked reduction of the range of  
394 these effects.

395 With these considerations in mind, we have proposed a plot strategy that enables these  
396 proximity effects to be largely circumvented. This strategy consists in generating patterns  
397 with a targeted small inter-structure distances through small displacements of a large inter-  
398 spot spacing DOE generated spot arrays. Despite the limited beam density in the fabrication  
399 area, imposing a compromise between DLW throughput and proximity effects, the proposed  
400 strategy represents an important step towards massively parallelized high-resolution  
401 additive fabrication. We have clearly illustrated that our strategy is efficient in bypassing  
402 proximity effects and thus in obtaining sub-micron resolution structures with high  
403 reproduction fidelity and greatly reduced fabrication times compared to the single beam  
404 approach.

405 Further studies would be interesting to extend the range of fabrication speeds, to fully  
406 understand the proximity effects in multi-photon DLW and determine the optimal writing  
407 speed ranges to completely suppress or at least control proximity effects. In particular, larger  
408 proximity effects have been reported for example when increasing the scanning speed for  
409 single-beam fabrication at significantly higher speeds ( $50 \text{ mm}\cdot\text{s}^{-1}$ ) (15) than used in our  
410 study.

411 We believe that the results presented in this paper and the consequent fabrication strategy  
412 will inspire further experimental and theoretical work in the parallel micro-fabrication of  
413 periodic structures with sub-micron motif separations.

## 417 **Materials and Methods**

### 418 **DOE preparation**

421 The spot array DOEs used to parallelise the write process were all designed using a modified  
422 three-stage Iterative Fourier Transform Algorithm (IFTA) (34–37). DOEs with different  
423 target images containing different numbers of output spots and different spots separations  
424 (corresponding to different DOE spatial periods and hence diffraction angles) were  
425 calculated and fabricated. Typical inter-spot diffraction angles ranged from  $1^\circ$  to  $0.01^\circ$ . The  
426 DOEs were all binary phase elements, etched into a layer (thickness  $\sim 400 \text{ nm}$ ) of spin-  
427 coated S1805 photoresist (MicroChem) on 1.1 mm thick float glass substrates using a

428 custom-built, massively parallel-write photoplotter (36, 37). Typical DOE experimental  
429 diffraction efficiencies of 70-75% were observed. When appropriate, target output spot  
430 patterns with a deliberately weakened central spot were chosen to compensate for increased  
431 zeroth order spot power resulting from inevitable DOE fabrication process limitations and  
432 hence obtain increased experimental array spot power uniformity. Occasionally, over-  
433 correction led to a slight underexposure of the central spot.

## 434 **Microfabrication**

435 *Resin preparation:* 1,10-decanediol diacrylate (DDA) was purchased from TCI,  
436 dipentaerythritol penta/hexa-acrylate (DPPHA) from Merck, unstabilized Ormocomp®  
437 from Micro Resist Technology GmbH, and 4-methoxyphenol (MEHQ) from Acros  
438 Organics. All reagents were used without further purification. Three resins were used in this  
439 study based on the use of a photoinitiator (PI) previously reported by our team (38, 39):  
440 PR\_organic (DPPHA/DDA/V-Shape, weight ratio: 79.2/19.8/1, includes *ca.* 600 ppm  
441 MEHQ as stabilizer/polymerization inhibitor), PR\_hybrid (PI-free Ormocomp/V-Shape,  
442 weight ratio: 99.5/0.5, stabilizer free) and stabilized PR\_hybrid (PI-free Ormocomp/V-  
443 Shape, weight ratio: 99.5/0.5 + 700 ppm MEHQ). In the first formulation PR\_organic  
444 (DPPHA/DDA/V-Shape, weight ratio: 79.2/19.8/1), V-Shape was mixed with 1,10-  
445 decanediol diacrylate (DDA) and stirred for 30 min at room temperature and then  
446 dipentaerythritol penta-/hexa-acrylate (DPPHA) was added without additional solvent  
447 (PR\_organic). The solution was stirred mechanically for 1 min and then magnetically for  
448 30 min.

449 For the second resin PR\_hybrid (PI-free Ormocomp/V-Shape, weight ratio: 99.5/0.5), the  
450 PI was mixed with a special PI-free Ormocomp resin and dichloromethane.  
451 Dichloromethane was allowed to evaporate overnight under stirring. Homogeneous resist  
452 was obtained without filtering.

453 The third formulation PR\_hybrid stabilized with 700 ppm MEHQ was made following the  
454 same procedure as PR\_hybrid but adding MEHQ along with V-Shape. Molecular structures  
455 are shown in Fig. 10

456  
457  
458  
459 **(Insert Figure 10)**

460  
461 *Fabrication and setup:* 3D microfabrication was performed on a Microlight3D printer  
462  $\mu$ FAB-3D based on a Zeiss Axiovert 200 inverted microscope equipped with a XYZ piezo  
463 nanomanipulator allowing the translation of the sample relative to the laser focal point, and  
464 a CMOS camera mounted behind a dichroic mirror to monitor the polymerization process.  
465 The laser module includes a microchip self-Q-switched frequency-doubled Nd:YAG laser  
466 (532 nm, 560 ps pulses, 11.7 kHz repetition rate, 11.5 mW maximum average power at the  
467 entrance of the microscope objective). Average laser powers were measured at the entrance  
468 pupil of the objective on a standard photodiode power sensor (S120VC, Thorlabs). The  
469 incident beam was focused with one of two different objectives ( $\times 100$ , NA 1.40, oil  
470 immersion, Zeiss Plan-APOCHROMAT and  $\times 40$ , NA 0.95, dry, Zeiss Plan-  
471 APOCHROMAT). The laser power, the displacement of the sample relative to the objective  
472 and the scanning speed were computer-controlled via LITHOS software. The DOEs were  
473 introduced at the entrance of the dichroic mirror cube in the reflector turret of the inverted  
474 microscope. The samples consist of resin drops disposed on borosilicate coverslips ( $170 \pm$   
475  $5 \mu\text{m}$  thick). After the fabrication process, the microstructures were finally obtained by  
476 washing away the unreacted monomer using acetone (two successive 10-minute baths).

477  
478 *Microstructure characterization:* Samples were metallized with a 5 nm thick gold coating  
479 via vacuum deposition with Leica EM ACE600 sputter coater and observed by Scanning  
480 Electron Microscopy (SEM) on a Zeiss Supra 55VP SEM operating at a tension of 5 kV,  
481 using a top view (0°) or a 45° view.  
482  
483

### 484 **Phenomenological digital simulations of the polymerization and diffusion processes**

485  
486 The parallelised write process, photo-chemical polymerization interactions and associated  
487 diffusion phenomena were modelled via digital simulations written in MATLAB, based on  
488 Point Spread Functions (PSF) calculated using the PSF Generator (40) software with the  
489 Gibson-Lanni model. The PSF represents the 3D light intensity distribution of the laser  
490 beam in the objective focal plane. Our software models the DOE generated light spot array  
491 as a 3D matrix of PSFs (Fig. S5).

492 The write process was modelled as the sequential, cumulative addition of several PSF  
493 arrays, one for each laser pulse, with a translation of the array between pulses as required to  
494 model the beam scanning process. Proximity effects between light spots were allowed for  
495 by introducing a diffusion step (convolution by a 3D Gaussian function) between each laser  
496 pulse. Several diffusion processes are possible, notably molecular diffusion such as radical  
497 or inhibitor diffusion (but heat energy brought by the laser and exothermic chemical  
498 interactions could also be involved). Our digital modelling of this diffusion is simplistic and  
499 purely phenomenological, making no *a priori* assumptions about the underlying physico-  
500 chemical mechanisms: we simply assume a diffusion process takes place, and calculations  
501 show that the characteristic lifetime of the diffusing species are compatible with values  
502 reported for carbon centred radical species. Polymerization was modelled by thresholding  
503 the cumulated light energy dose during the process, applying non-linear functions as  
504 required to represent multi-photon processes. A sampling grid of 200 nm was chosen as a  
505 compromise between maintaining manageable computing loads and modelling the PSF  
506 functions with sufficient fidelity. Supplementary details regarding mathematical simulation  
507 and parameters are featured as SI.  
508  
509  
510

### 511 **References**

- 512 1. S. C. Ligon, R. Liska, J. Stampfl, M. Gurr, R. Mülhaupt, Polymers for 3D Printing and  
513 Customized Additive Manufacturing. *Chem. Rev.* **117**, 10212–10290 (2017).
- 514 2. S. Maruo, J. T. Fourkas, Recent progress in multiphoton microfabrication. *Laser Photonics*  
515 *Rev.* **2**, 100–111 (2008).
- 516 3. C. Barner-Kowollik, M. Bastmeyer, E. Blasco, G. Delaittre, P. Müller, B. Richter, M.  
517 Wegener, 3D Laser Micro- and Nanoprinting: Challenges for Chemistry. *Angew. Chem. Int.*  
518 *Ed.* **56**, 15828–15845 (2017).
- 519 4. J. Kato, N. Takeyasu, Y. Adachi, H.-B. Sun, S. Kawata, Multiple-spot parallel processing  
520 for laser micronanofabrication. *Appl. Phys. Lett.* **86**, 044102 (2005).

- 521 5. C. S. Lim, M. H. Hong, Y. Lin, Q. Xie, B. S. Luk'yanchuk, A. Senthil Kumar, M. Rahman,  
522 Microlens array fabrication by laser interference lithography for super-resolution surface  
523 nanopatterning. *Appl. Phys. Lett.* **89**, 191125 (2006).
- 524 6. H. Lin, B. Jia, M. Gu, Dynamic generation of Debye diffraction-limited multifocal arrays for  
525 direct laser printing nanofabrication. *Opt. Lett.* **36**, 406–408 (2011).
- 526 7. H. Ren, H. Lin, X. Li, M. Gu, Three-dimensional parallel recording with a Debye  
527 diffraction-limited and aberration-free volumetric multifocal array. *Opt. Lett.* **39**, 1621–1624  
528 (2014).
- 529 8. P. S. Salter, M. J. Booth, Addressable microlens array for parallel laser microfabrication.  
530 *Opt. Lett.* **36**, 2302–2304 (2011).
- 531 9. K. Obata, J. Koch, U. Hinze, B. N. Chichkov, Multi-focus two-photon polymerization  
532 technique based on individually controlled phase modulation. *Opt. Express.* **18**, 17193–  
533 17200 (2010).
- 534 10. S. D. Gittard, A. Nguyen, K. Obata, A. Koroleva, R. J. Narayan, B. N. Chichkov,  
535 Fabrication of microscale medical devices by two-photon polymerization with multiple foci  
536 via a spatial light modulator. *Biomed. Opt. Express.* **2**, 3167–3178 (2011).
- 537 11. G. Vizsnyiczai, L. Kelemen, P. Ormos, Holographic multi-focus 3D two-photon  
538 polymerization with real-time calculated holograms. *Opt. Express.* **22**, 24217–24223 (2014).
- 539 12. Q. Geng, D. Wang, P. Chen, S.-C. Chen, Ultrafast multi-focus 3-D nano-fabrication based  
540 on two-photon polymerization. *Nat. Commun.* **10**, 2179 (2019).
- 541 13. V. Hahn, P. Kiefer, T. Frenzel, J. Qu, E. Blasco, C. Barner-Kowollik, M. Wegener, Rapid  
542 Assembly of Small Materials Building Blocks (Voxels) into Large Functional 3D  
543 Metamaterials. *Adv. Funct. Mater.* **30**, 1907795 (2020).
- 544 14. L. Zheng, K. Kurselis, A. El-Tamer, U. Hinze, C. Reinhardt, L. Overmeyer, B. Chichkov,  
545 Nanofabrication of High-Resolution Periodic Structures with a Gap Size Below 100 nm by  
546 Two-Photon Polymerization. *Nanoscale Res. Lett.* **14**, 134 (2019).
- 547 15. J. S. Oakdale, R. F. Smith, J.-B. Forien, W. L. Smith, S. J. Ali, L. B. B. Aji, T. M. Willey, J.  
548 Ye, A. W. van Buuren, M. A. Worthington, S. T. Prisbrey, H.-S. Park, P. A. Amendt, T. F.  
549 Baumann, J. Biener, Direct Laser Writing of Low-Density Interdigitated Foams for Plasma  
550 Drive Shaping. *Adv. Funct. Mater.* **27**, 1702425 (2017).
- 551 16. E. Waller, G. von Freymann, Spatio-Temporal Proximity Characteristics in 3D  $\mu$ -Printing  
552 via Multi-Photon Absorption. *Polymers.* **8**, 297 (2016).
- 553 17. S. H. Park, T. W. Lim, D.-Y. Yang, N. C. Cho, K.-S. Lee, Fabrication of a bunch of sub-30-  
554 nm nanofibers inside microchannels using photopolymerization via a long exposure  
555 technique. *Appl. Phys. Lett.* **89**, 173133 (2006).
- 556 18. D. Tan, Y. Li, F. Qi, H. Yang, Q. Gong, X. Dong, X. Duan, Reduction in feature size of two-  
557 photon polymerization using SCR500. *Appl. Phys. Lett.* **90**, 071106 (2007).

- 558 19. Y. Bougdid, I. Maouli, A. Rahmouni, K. Mochizuki, I. Bennani, M. Halim, Z. Sekkat,  
559 Systematic  $\lambda/21$  resolution achieved in nanofabrication by two-photon-absorption  
560 induced polymerization. *J. Micromech. Microeng.* **29**, 035018 (2019).
- 561 20. J. B. Mueller, J. Fischer, F. Mayer, M. Kadic, M. Wegener, Polymerization Kinetics in  
562 Three-Dimensional Direct Laser Writing. *Adv. Mater.* **26**, 6566–6571 (2014).
- 563 21. L. Yang, A. Münchinger, M. Kadic, V. Hahn, F. Mayer, E. Blasco, C. Barner-Kowollik, M.  
564 Wegener, On the Schwarzschild Effect in 3D Two-Photon Laser Lithography. *Adv. Opt.*  
565 *Mater.* **7**, 1901040 (2019).
- 566 22. X. Wan, R. Menon, Proximity-effect correction for 3D single-photon optical lithography.  
567 *Appl. Opt.* **55**, A1–A7 (2016).
- 568 23. M. T. Do, T. T. N. Nguyen, Q. Li, H. Benisty, I. Ledoux-Rak, N. D. Lai, Submicrometer 3D  
569 structures fabrication enabled by one-photon absorption direct laser writing. *Opt. Express.*  
570 **21**, 20964–20973 (2013).
- 571 24. S. Rodríguez, Redefining Microfabrication of High-Precision Optics. *PhotonicsViews.* **17**,  
572 36–39 (2020).
- 573 25. L. Jiang, W. Xiong, Y. Zhou, Y. Liu, X. Huang, D. Li, T. Baldacchini, L. Jiang, Y. Lu,  
574 Performance comparison of acrylic and thiol-acrylic resins in two-photon polymerization.  
575 *Opt. Express.* **24**, 13687–13701 (2016).
- 576 26. S. K. Saha, C. Divin, J. A. Cuadra, R. M. Panas, Effect of Proximity of Features on the  
577 Damage Threshold During Submicron Additive Manufacturing Via Two-Photon  
578 Polymerization. *J Micro Nanomanuf.* **5**, 031002 (2017).
- 579 27. S. K. Saha, D. Wang, V. H. Nguyen, Y. Chang, J. S. Oakdale, S.-C. Chen, Scalable  
580 submicrometer additive manufacturing. *Science.* **366**, 105–109 (2019).
- 581 28. F. Hilbert, J. Wiedenmann, B. Stender, W. Mantei, R. Houbertz, Q. Carlier, L. P.  
582 Covarrubias, K. Heggarty, C. Arnoux, C. Monnereau, P. Baldeck, Impact of massive  
583 parallelization on two-photon absorption micro- and nanofabrication, Proc. SPIE 11271,  
584 Laser 3D Manufacturing VII, 1127105 (2020).
- 585 29. D. Griller, K. U. Ingold, Persistent carbon-centered radicals. *Acc. Chem. Res.* **9**, 13–19  
586 (1976).
- 587 30. J. Wen, Y. Zhang, M. Xiao, The Talbot effect: recent advances in classical optics, nonlinear  
588 optics, and quantum optics. *Adv. Opt. Photon.* **5**, 83–130 (2013).
- 589 31. H. H. Solak, C. Dais, F. Clube, Displacement Talbot lithography: a new method for high-  
590 resolution patterning of large areas. *Opt. Express.* **19**, 10686–10691 (2011).
- 591 32. P.-M. Coulon, B. Damilano, B. Alloing, P. Chausse, S. Walde, J. Enslin, R. Armstrong, S.  
592 Vézian, S. Hagedorn, T. Wernicke, J. Massies, J. Zúñiga-Pérez, M. Weyers, M. Kneissl, P.  
593 A. Shields, Displacement Talbot lithography for nano-engineering of III-nitride materials.  
594 *Microsyst. Nanoeng.* **5**, 1–12 (2019).

- 595 33. D. J. Shir, S. Jeon, H. Liao, M. Highland, D. G. Cahill, M. F. Su, I. F. El-Kady, C. G.  
596 Christodoulou, G. R. Bogart, A. V. Hamza, J. A. Rogers, Three-Dimensional  
597 Nanofabrication with Elastomeric Phase Masks. *J. Phys. Chem. B.* **111**, 12945–12958  
598 (2007).
- 599 34. O. Ripoll, V. Kettunen, H. P. Herzig, Review of iterative Fourier-transform algorithms for  
600 beam shaping applications. *Opt. Express.* **43**, 2549–2548 (2004).
- 601 35. F. Wyrowski, Iterative quantization of digital amplitude holograms. *Appl. Opt., AO.* **28**,  
602 3864–3870 (1989).
- 603 36. M. M. Kessels, M. E. Bouz, R. Pagan, K. J. Heggarty, Versatile stepper based maskless  
604 microlithography using a liquid crystal display for direct write of binary and multilevel  
605 microstructures. *J Micro Nanolithogr MEMS MOEMS.* **6**, 033002 (2007).
- 606 37. M. V. Kessels, C. Nassour, P. Grosso, K. Heggarty, Direct write of optical diffractive  
607 elements and planar waveguides with a digital micromirror device based UV photoplotter.  
608 *Opt. Commun.* **283**, 3089–3094 (2010).
- 609 38. C. Arnoux, T. Konishi, E. Van Elslande, E.-A. Poutougnigni, J.-C. Mulatier, L. Khrouz, C.  
610 Bucher, E. Dumont, K. Kamada, C. Andraud, P. Baldeck, A. Banyasz, C. Monnereau,  
611 Polymerization Photoinitiators with Near-Resonance Enhanced Two-Photon Absorption  
612 Cross-Section: Toward High-Resolution Photoresist with Improved Sensitivity.  
613 *Macromolecules.* **53**, 9264–9278 (2020).
- 614 39. J. Rouillon, C. Arnoux, C. Monnereau, Determination of Photoinduced Radical Generation  
615 Quantum Efficiencies by Combining Chemical Actinometry and <sup>19</sup>F NMR Spectroscopy.  
616 *Anal. Chem.* **93**, 2926–2932 (2021).
- 617 40. BIG • PSF Generator, (available at <http://bigwww.epfl.ch/algorithms/psfgenerator/>).

618  
619

## 620 Acknowledgments

621

622 The authors thank Fabian Hilbert (Multiphoton Optics GmbH) and Ruth Houbertz  
623 (ThinkMade Engineering & Consulting i.Gr.) for inspiring discussions.

624

## 625 Funding:

626 ENS Lyon authors acknowledge the Agence Nationale de la Recherche ANR for the grant  
627 “New 3D print”, especially C.A for doctoral grant.

628 This work has received funding from the European Union’s Horizon 2020 research and  
629 innovation program under grant agreement N° 780278. The dissemination of results herein  
630 reflects only the author’s view and the European Commission is not responsible for any  
631 use that may be made of the information it contains.

632

## 633 Author contributions:

634

635 Examples:  
636 Conceptualization: CA, PLB, AK, CM, KH,  
Methodology: CA, AB, CM, KH, QC

Investigation: CA, AB, KH, LPC  
Visualization: CA, AB, LPC  
Supervision: AB, CM, KH, AK  
Writing—original draft: CA, AB, CM, KH, LPC  
Writing—review & editing: CM, KH, AK, LPC

**Competing interests:** All authors declare they have no competing interests.

**Data and materials availability:** All data are available in the main text or the supplementary materials.

## Figures and Tables

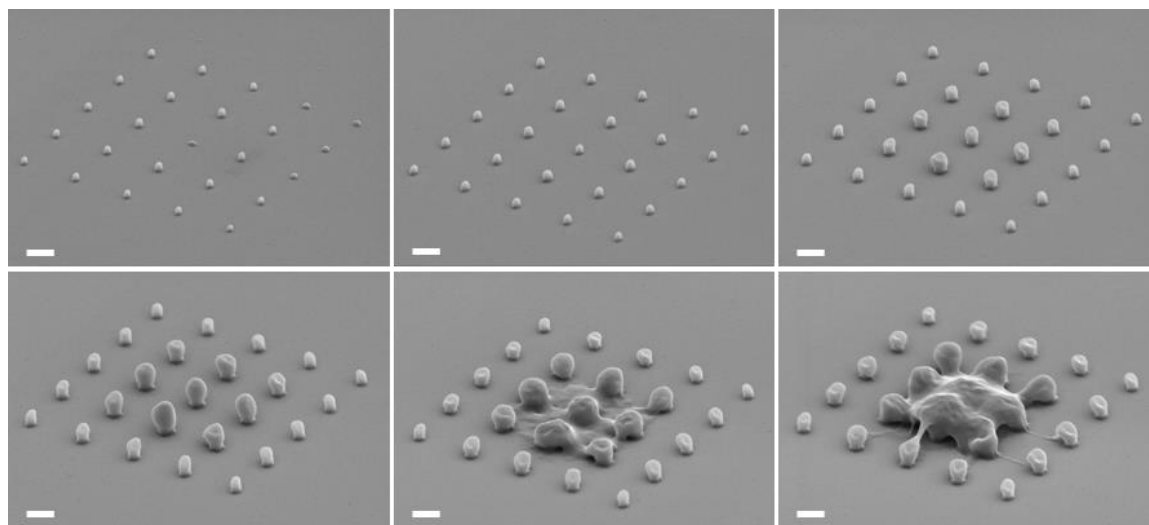
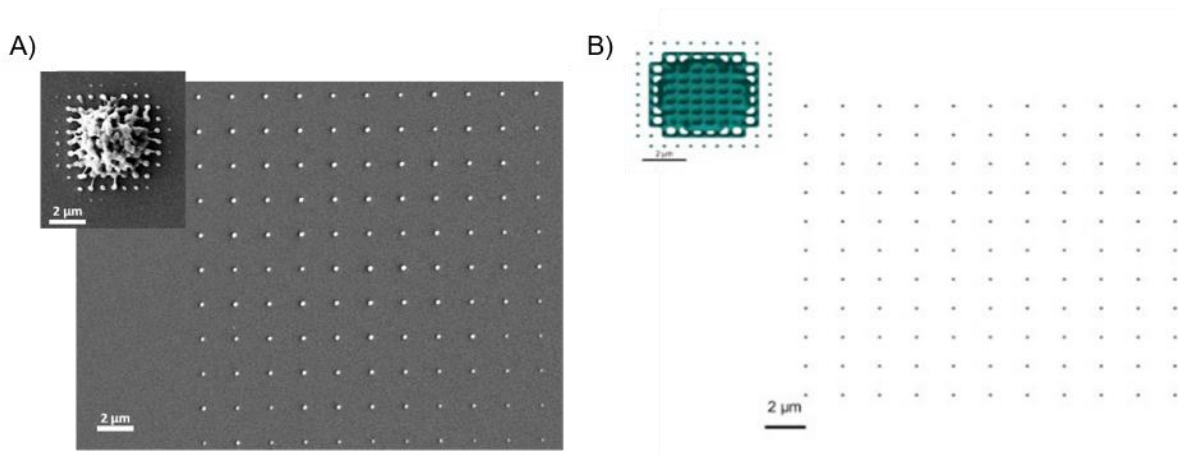
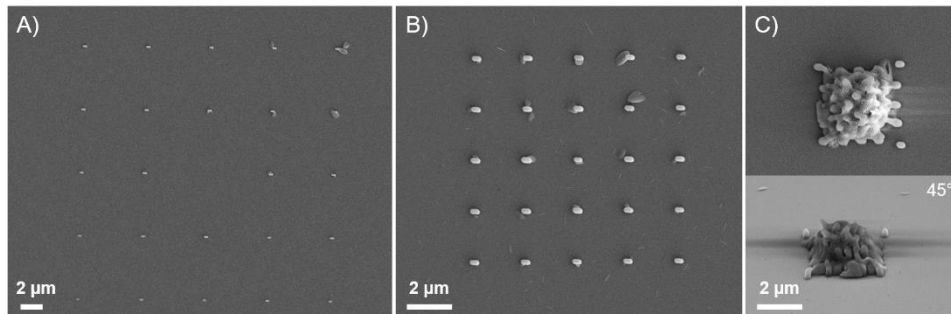


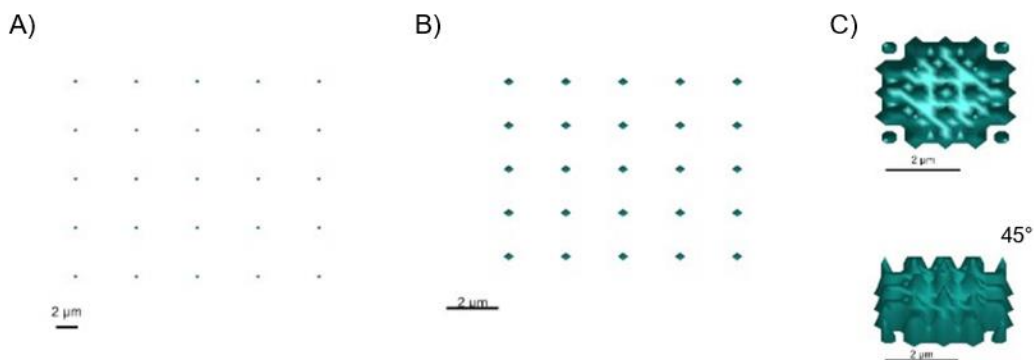
**Fig. 1. Illustration of the proximity effects on a voxel array manufactured in PR\_HybridOrmocomp/V-Shape with a 5×5 spot DOE with an inter-spot distance of 2.22 μm with increasing total laser power (top line, from left to right: 1.9 – 2.6 – 3.5 mW; bottom line, from left to right: 4.0 – 4.4 – 4.8 mW). Exposure time is constant (100 ms). Scale bar: 1 μm.**



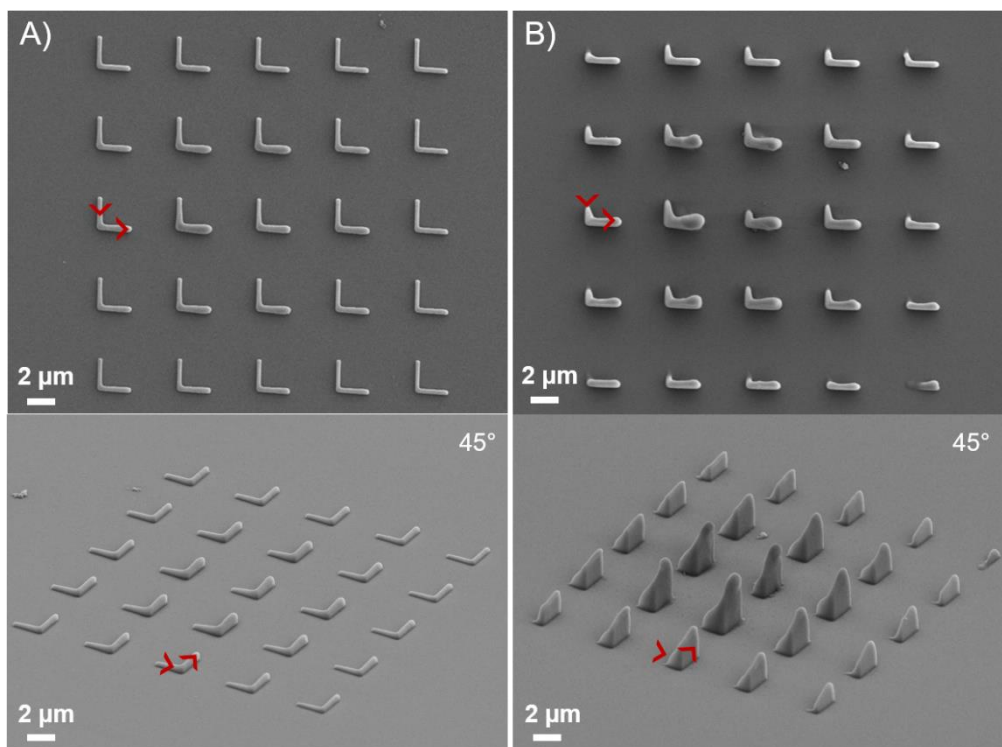
658  
 659 **Fig. 2. (A) Voxel arrays manufactured in the PR\_organic resin with two 11×11 spot**  
 660 **DOEs with inter-spot distances of 0.62 μm (insert top left) and 1.85 μm (right) at 5.4**  
 661 **mW total average incident laser power on the DOE using the 100× objective. The**  
 662 **exposure times were 50 ms and 5 s for the 0.62 μm and 1.85 μm spacings respectively.**  
 663 **(B) Results of the digital simulation (including diffusion) of the parallel DLW process,**  
 664 **showing the effect of spot distance, for voxel arrays manufactured in the PR\_organic**  
 665 **resin with two 11×11 spot DOEs with diffusion. The inter-spot distances are 0.6 μm**  
 666 **(insert top left) and 1.8 μm (right).**



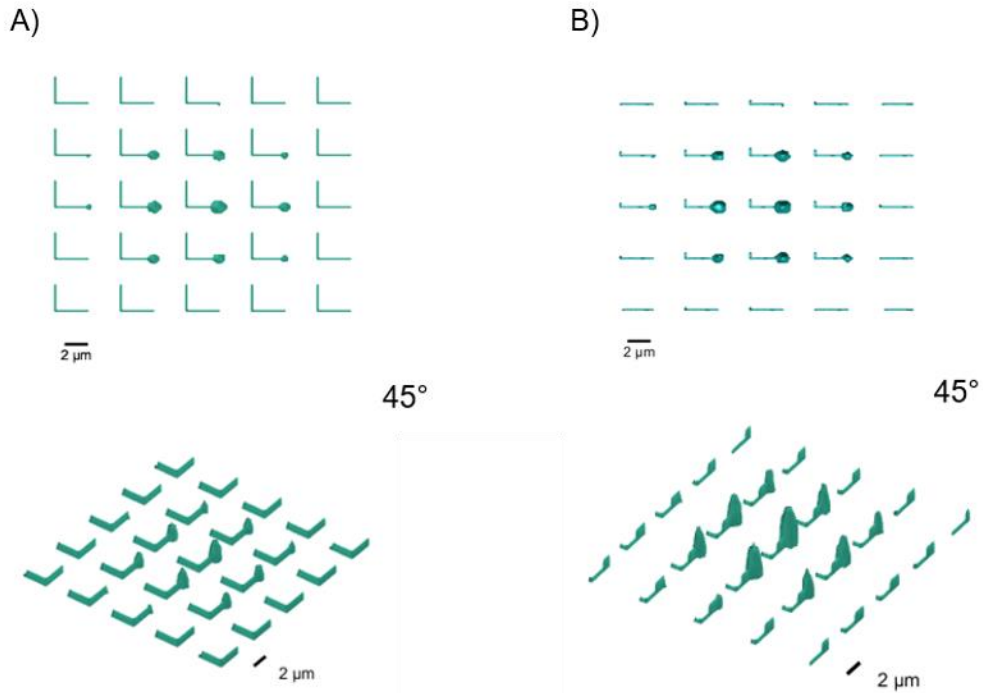
669  
 670 **Fig. 3. Arrays of voxels manufactured with three 5×5 spot DOEs at decreasing inter-**  
 671 **spot distance. Spacing from left to right: (A) 5.55, (B) 2.22, (C) 0.89 μm.  $P_{total} = 4.0$**   
 672 **mW, exposure time: 50 ms. Resin: PR\_organic. 100× objective.**



675  
676 **Fig. 4. Results of the digital simulation of the parallel write process showing of the**  
677 **effect of spot separation for 5×5 arrays. (A) 5.6 μm, (B) 2.2 μm and (C) 0.8 μm. Total**  
678 **number of laser pulses was 585 in each case.**

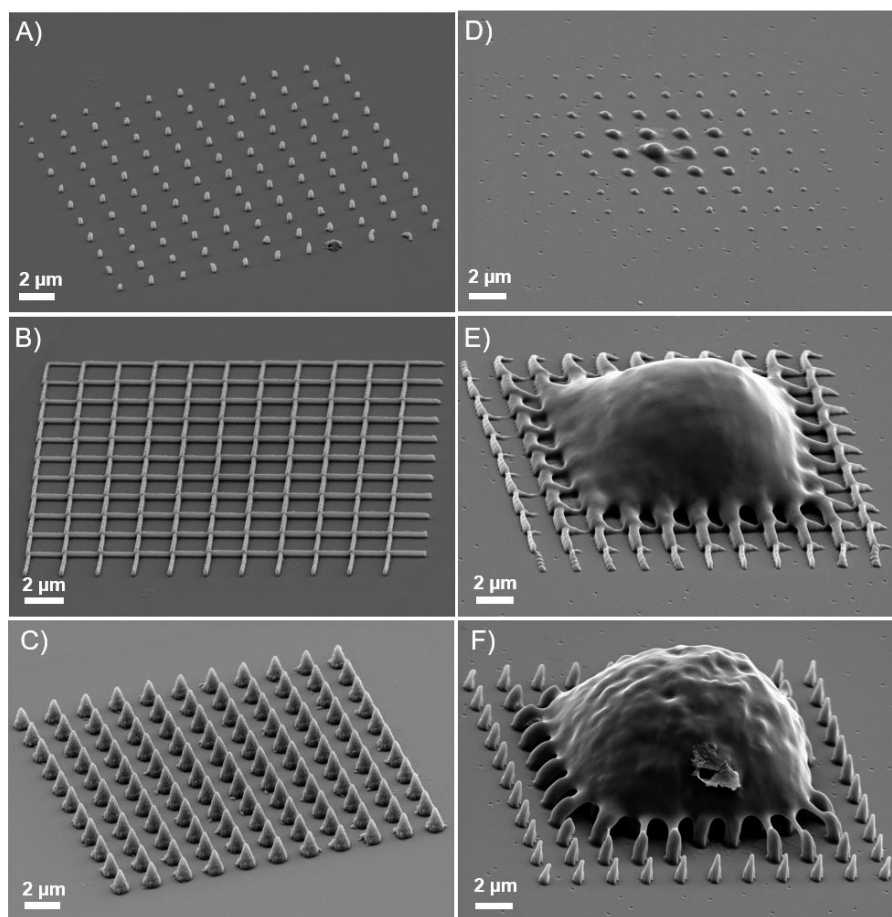


681  
682 **Fig. 5. Influence of the microscope objective on the uniformity of 5×5 "L" networks (2**  
683 **μm per arm) separated by 5.55 μm. (A) Objective 100× (NA 1.40),  $P_{total} = 3$  mW,  $v =$**   
684  **$2.4 \mu\text{m}\cdot\text{s}^{-1}$ . (B) Objective 40× (NA 0.95),  $P_{total} = 9.0$  mW,  $v = 2.4 \mu\text{m}\cdot\text{s}^{-1}$ . Resin:**  
685 **PR\_hybrid. For each array, top (top) and 45° (bottom) views are shown and the**  
686 **writing direction is marked by red arrows. The structures of network (A) are fairly**  
687 **uniform while those of network (B) show important disparities.**



690  
 691 **Fig. 6. Results of the digital simulations of the scanned spot array write process**  
 692 **showing the influence of the objective NA on the uniformity of 5×5 “L” networks. (A)**  
 693 **NA 0.95, (B) NA 1.40. Top (top) and 45° (bottom) views are shown for each structure.**

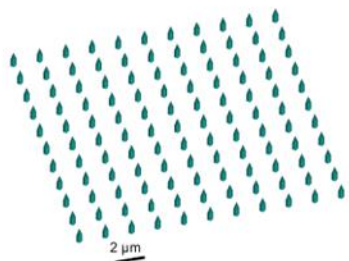
694  
 695



696 **Fig. 7. Effect of resin monomer on the written structures: voxel structure arrays (top),**  
 697 **“L” shapes (center) and cones arrays (bottom) manufactured with an 11×11 spot DOE.**  
 698 **Left: PR\_organic resin, spacing: 1.85 μm.  $P_{total} = 5.4$  mW, 100× objective, exposure**  
 699 **time: (A) 5 s and scanning speeds: (B)  $120 \text{ nm.s}^{-1}$  and (C)  $240 \text{ nm.s}^{-1}$ .** **Right: PR\_hybrid,**  
 700 **spacing: 1.85 μm.  $P_{total} = 5.4$  mW, 100× objective, exposure time: (D) 50 ms and**  
 701 **scanning speeds: (E)  $40 \text{ μm.s}^{-1}$  and, (F)  $120 \text{ μm.s}^{-1}$ .**  
 702

696  
 697  
 698  
 699  
 700  
 701  
 702  
 703  
 704

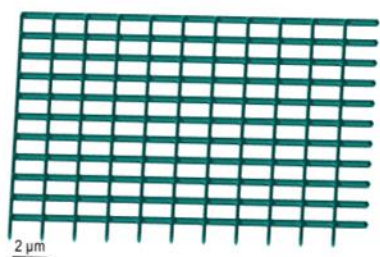
A)



D)



B)



E)

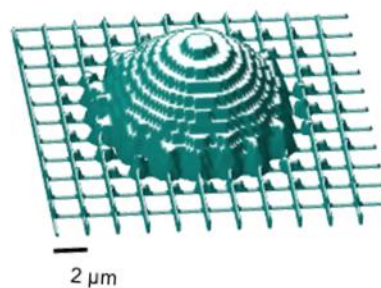
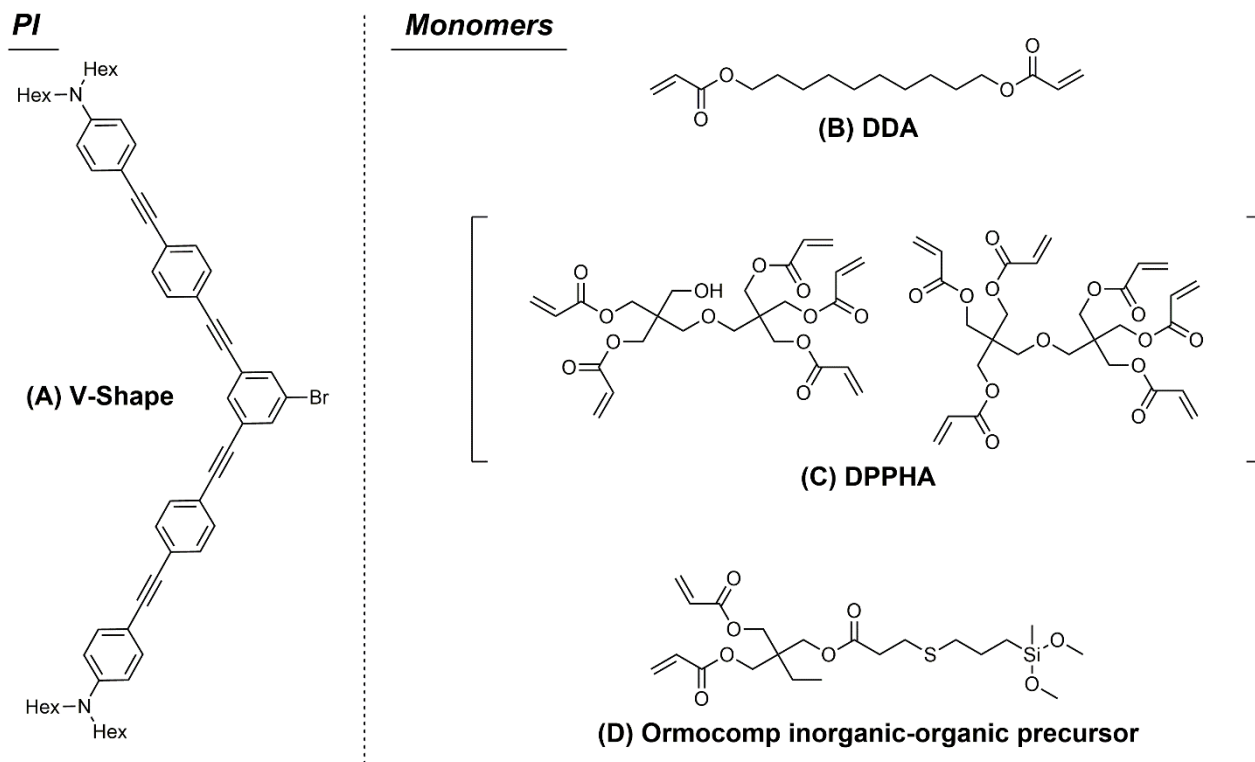


**Fig. 8. Results of the digital simulation of the parallel-write process, showing of the effect of resin monomer properties on the structures obtained for voxel structure arrays (top) and “L” shapes (bottom). (Left: PR\_organic resin, Right: PR\_hybrid). Cones were not simulated due to computational load.**

Fabrication strategies	Total fabrication time	Motif	SEM pictures of an array of 900 voxels separated by 0.9 μm	
(A) With DOE Spacing 0.89 μm	22.5 s			
(B) With DOE Spacing 5.55 μm	22.5 s			
(C) Without DOE	9 min 18.2 s			

713 **Fig. 9.** Comparison of two parallel and one non-parallel printing strategies for the  
 714 fabrication of a 900 (30×30) voxel structure array with an inter-structure distance of  
 715 *ca.* 0.9 μm: (A) with a DOE spot array period of 0.9 μm, (B) with a DOE spot array  
 716 period of 5.55 μm, (C) without a DOE, point by point writing (reference). Objective  
 717 100×, Photoresist: PR\_hybrid. Exposure time for each individual voxel structure: 10  
 718 ms. (A)  $P_{\text{total}} = 4.4 \text{ mW}$ ; (B)  $P_{\text{total}} = 4.4 \text{ mW}$ ; (C)  $P = 123 \text{ μW}$ .



721  
722 **Fig. 10.** Chemical structures of the PI and the monomers used in this study: (A) V-  
 723 Shape (38, 39); (B) 1,10-decanediol diacrylate DDA; (C) dipentaerythritol penta/hexa-  
 724 acrylate DPPHA; (D) Ormocomp is an organic-inorganic hybrid network based on the  
 725 precursor mentioned herein.

## Supplementary Materials for **Understanding and Overcoming Proximity Effects in Multi-Spot Two-Photon Direct Laser Writing**

Caroline Arnoux,\* Luis A. Pérez-Covarrubias, Alexandre Khaldi, Quentin Carlier, Patrice L. Baldeck, Kevin. Heggarty,\* Akos Banyasz and Cyrille Monnereau

\*Corresponding authors. Email: [c.caroline.arnoux@gmail.com](mailto:c.caroline.arnoux@gmail.com) ; [kevin.heggarty@imt-atlantique.fr](mailto:kevin.heggarty@imt-atlantique.fr)

### **This PDF file includes:**

Supplementary Text  
Tables S1  
Figs. S1 to S5

### **Other Supplementary Materials for this manuscript include the following:**

Movies S1-S4

## Supplementary Text

### Full details of the mathematical model used in the MatLab simulation

The two-photon DLW process was modelled by assuming that each laser pulse generates a quasi-instantaneous 3D spatial distribution of reactive species ( $r^{\text{inst}}$ ) which corresponds to the exposed PSF spot array. The polymerized structures are the result of sequential, cumulative addition of reactive species distributions, one for each laser pulse.

The distribution of the reactive species during the laser exposure was modeled by the following recursive convolution algorithm:

$$r^{(k)} = d \otimes (r^{(k-1)} + r^{\text{inst}}) \cdot q, \quad (1)$$

where  $r^{(k-1)}$  and  $r^{(k)}$  stand for the spatial distribution of accumulated reactive species after the  $(k-1)^{\text{th}}$  and  $k^{\text{th}}$  laser pulses, respectively. The spatial coordinates are omitted for simplicity. The function  $d$  stands for the effective diffusion function described by a Gaussian spatial distribution presented only for 1D:

$$d(x) = N e^{\frac{-x^2}{2\sigma^2}}. \quad (2)$$

The standard deviation parameter  $\sigma$  is proportional to the width of the Gaussian function. The spatial distribution of the reactive species  $r^{(k)}$  after  $k^{\text{th}}$  laser pulse is obtained by convolving the diffusion function  $d$ , with the sum of the accumulated reactive species  $r^{(k-1)}$  generated by the preceding laser pulses and the reactive species generated by the  $k^{\text{th}}$  pulse  $r^{\text{inst}}$ .  $N$  is a normalization factor.

The consumption of the reactive species was taken into account by the decay parameter  $q$ , whose value is lower than 1, typically from 0.99 to 0.99999. Finally, the beam scanning process was included into the model by spatially translating the  $r^{\text{inst}}$  from one laser pulse to another.

As can be seen from equation 1, we assume that each laser pulse generates the same quantity of radicals, thus the eventual depletion of PI is not considered. Furthermore, the effective diffusion remains constant during the accumulation of laser pulses.

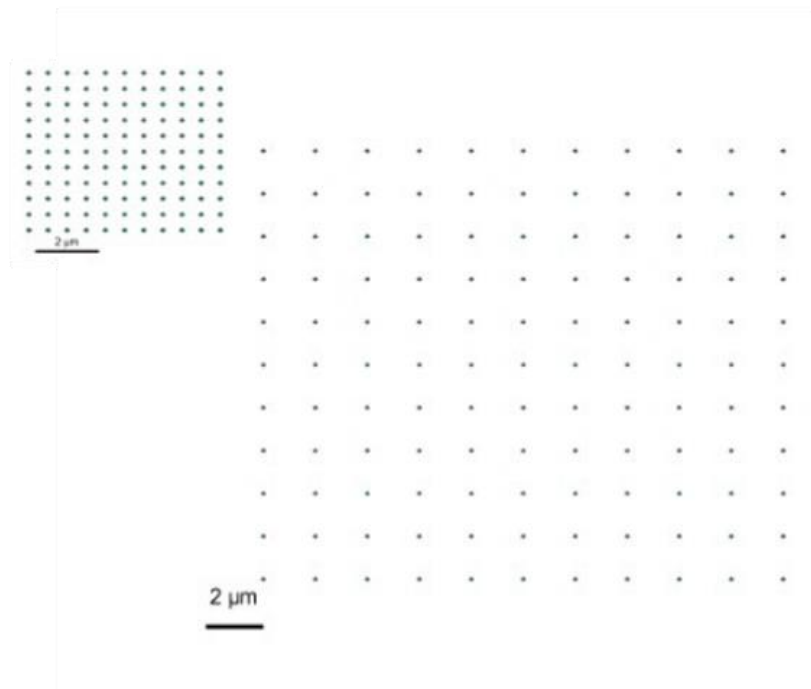
Polymerization was modelled by thresholding the cumulated light energy dose during the process: any zone (any sampling voxel) of the accumulated 3D spatial distribution,  $r^{(k)}$ , whose value was above an empirically chosen threshold value was considered polymerised. Multi-photon non-linear effects were represented by applying non-linear functions as required to the PSF spot light distribution and so equivalently on the quasi-instantaneous 3D spatial distribution of reactive species ( $r^{\text{inst}}$ ).

To implement the above algorithm using a 3D convolution, a sampling grid of 200 nm was chosen as a compromise between maintaining manageable computing loads and modelling the PSF functions with sufficient fidelity. The calculated accumulated 3D spatial distribution was convolved by a Gaussian diffusion kernel between each laser pulse using the Matlab smooth3 function. The  $\sigma$  parameter of the Gaussian kernel was optimized empirically through repeated simulations to give an acceptable fit to the experimentally obtained structures. The kernel size was adapted to minimize computational load while maintaining an acceptable precision in the sampling of the Gaussian convolution function. The same kernel size and  $\sigma$  parameters (summarized in Table 1) were used for a given photoresist to maintain simulation coherence.

Photoresist	kernel size (XYZ)	$\sigma$	q
PR_organic	1×1×3 voxels	0.5	0.995
PR_hybrid	3×3×7 voxels	1.8	0.99999

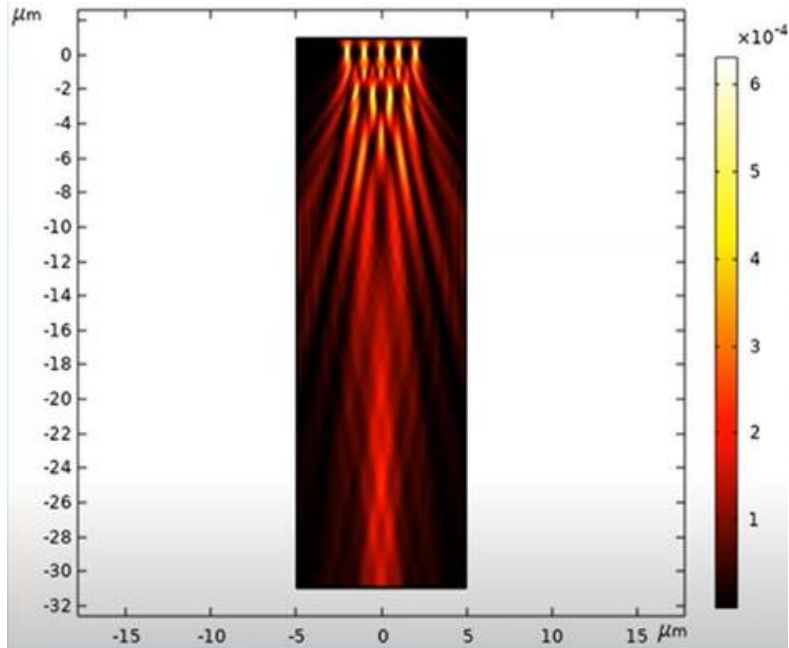
**Table S1.**

Summary of the size,  $\sigma$ -value of the Gaussian convolution kernel and decay factor q used to simulate diffusion effects in the different resists



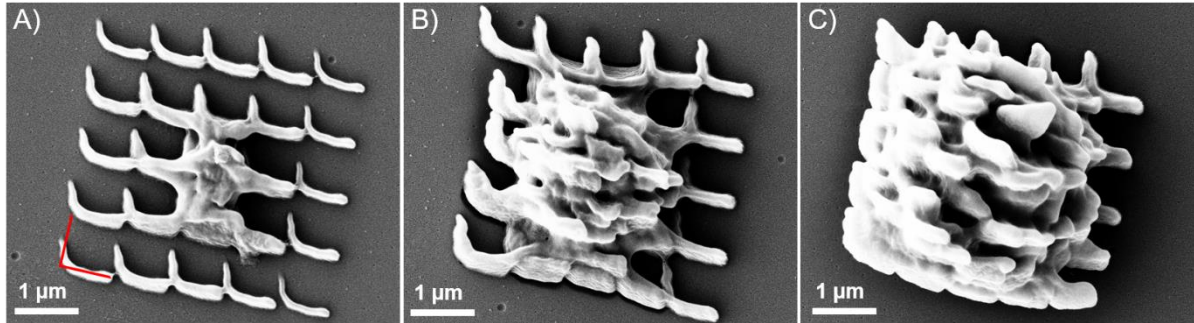
**Fig. S1.**

Results of the digital simulation of the parallel write process showing of the effect of spot separation for voxel structure arrays manufactured in the PR\_organic resin using two 11×11 spot DOEs when diffusion is not taken into account.



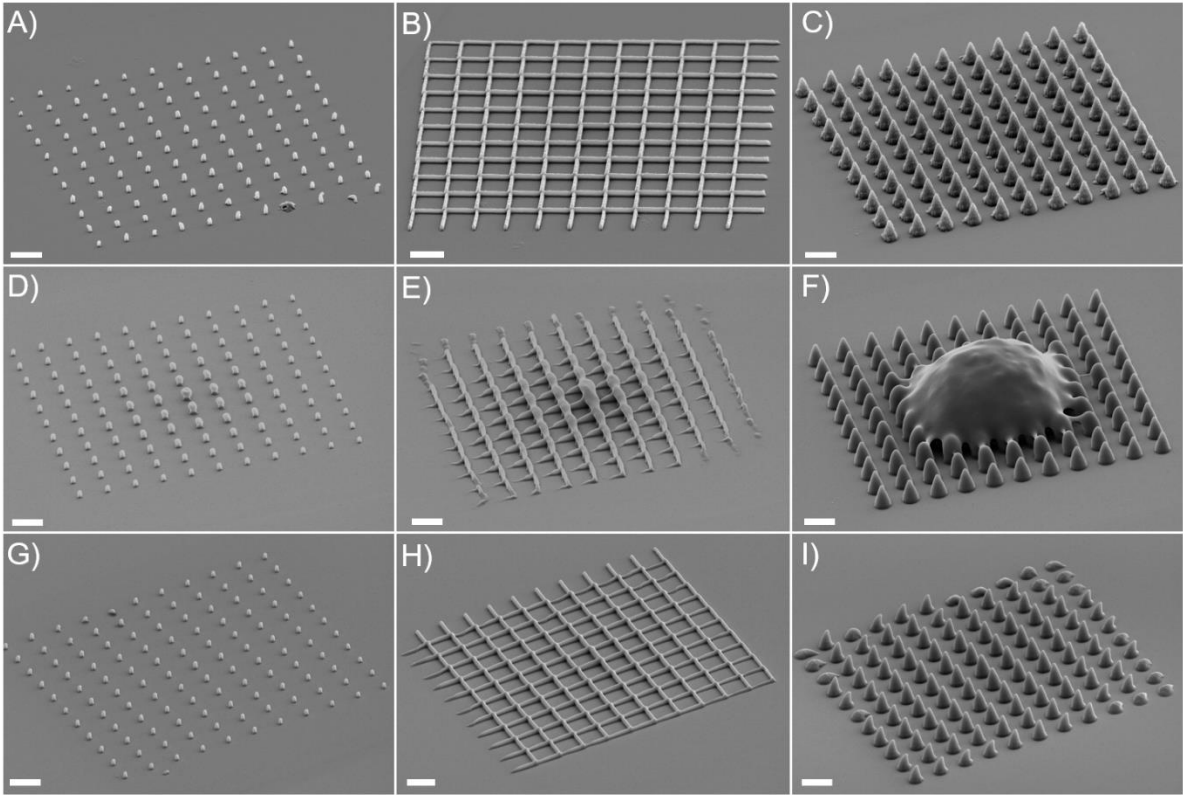
**Fig. S2.**

Simulation of the light distribution in planes beyond the focal plane (plane  $z = 0$  at the top of the figure) for a  $1 \times 5$  spot array showing the presence of Talbot effect like “hot spots” outside the focal plane. Note that this simulation was for light spots with identical light phases.



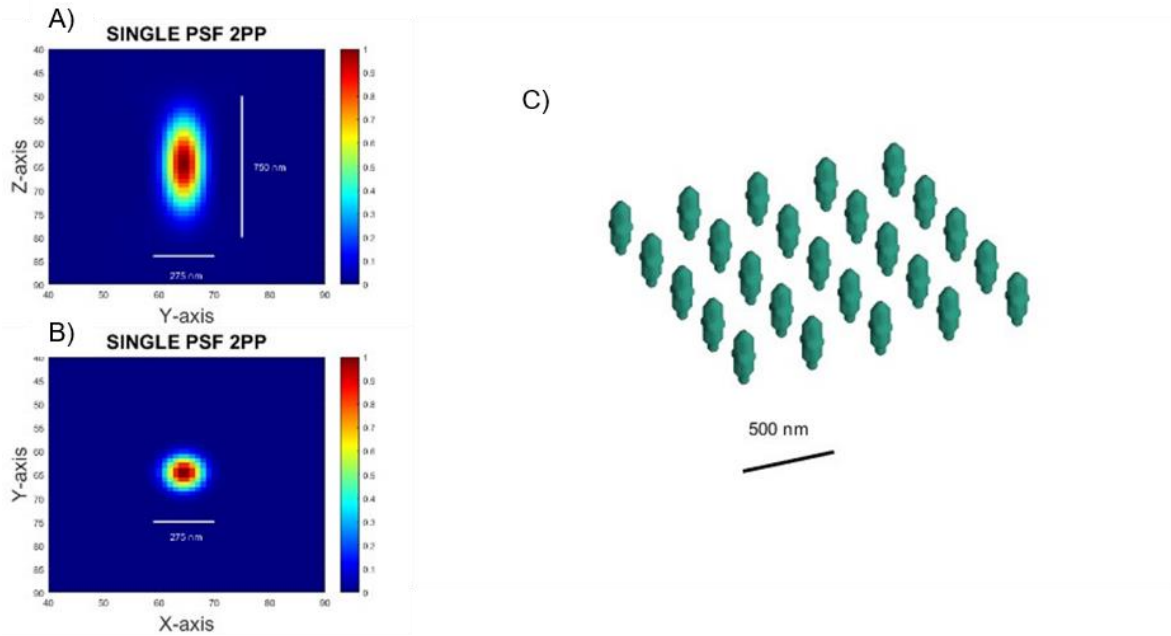
**Fig. S3.**

Illustration of the influence of out-of-plane “hot spots” resulting from the interference between the incident light “beams” as they propagate to form the array spots: distortion of arrays of L-shaped structures (depicted in red in the left picture) at a small ( $0.89\ \mu\text{m}$ ) inter-spot spacing manufactured by using a  $5\times 5$  spot DOE and a  $100\times$  objective at a total incident laser power of (A) 2.7, (B) 3.7 and (C) 5.0 mW. Scanning speed:  $40\ \mu\text{m}\cdot\text{s}^{-1}$ . Resin: PR\_organic. A multi-layer structuring is clearly apparent, but is noticeably different to the structuring resulting from proximity effects at larger inter-spot distances.



**Fig. S4.**

Experimental results for a  $11 \times 11$  spot, parallel write process: voxel array structures (A, D, G), “L” (B, E, H) and cones (C, F, I) using either PR-organic (A, B, C), PR\_hybrid (D, E, F) or PR\_hybrid stabilized with 700 ppm MEHQ (H, I, J). Individual fabrication conditions are as follow. A:  $P_{\text{total}} = 5.4 \text{ mW}$ ,  $t_{\text{exp}} = 5 \text{ s}$ ; B:  $P_{\text{total}} = 5.4 \text{ mW}$ ,  $v = 0.12 \mu\text{m.s}^{-1}$ ; C:  $P_{\text{total}} = 5.4 \text{ mW}$ ,  $v = 0.24 \mu\text{m.s}^{-1}$ ; D:  $P_{\text{total}} = 4.4 \text{ mW}$ ,  $t_{\text{exp}} = 2 \text{ s}$ ; E:  $P_{\text{total}} = 4.4 \text{ mW}$ ,  $v = 1.7 \mu\text{m.s}^{-1}$ ; F:  $P_{\text{total}} = 4.4 \text{ mW}$ ,  $v = 2.4 \mu\text{m.s}^{-1}$ ; G:  $P_{\text{total}} = 4.4 \text{ mW}$ ,  $t_{\text{exp}} = 5 \text{ s}$ ; H:  $P_{\text{total}} = 4.4 \text{ mW}$ ,  $v = 0.17 \mu\text{m.s}^{-1}$ ; I:  $P_{\text{total}} = 4.4 \text{ mW}$ ,  $v = 1.2 \mu\text{m.s}^{-1}$ . Scale bar:  $2 \mu\text{m}$ .



**Fig. S5.**

Numerical simulations of the Point Spread Function (PSF) for a 100 $\times$  NA 1.40 microscope objective. (A) Intensity distribution of one PSF in the YZ plane, (B) intensity distribution of one PSF in the XY plane. (C) Polymerized areas of a 5 $\times$ 5 PSF array at a fixed threshold value (here a sampling grid of 25 nm has been used for visualization purposes).

**Movie S1-S4.**

Example video animations showing the temporal progress of the digital simulations of the multi-spot write process. Movies S1, S2, and S3 are for static 5x5 spot arrays in the PR\_organic resist. S4 is for an 11x11 spot array scanned in an L shape in the PR\_hybrid resist. In all figures the X and Y dimensions indicated are in sampling grid units: one unit is 200nm.

Spot separations are S1:5.6 $\mu$ m, S2:2.2 $\mu$ m, S3:0.8 $\mu$ m, S4:1.8 $\mu$ m.

As each simulation progresses, we can see the “energy dose” (or equivalently the hypothesized radical spatial density) build up in the center of each write spot and the diffusion of this dose into the immediate vicinity of the spot. For small spot separations or high diffusion resists, this diffusion leads to proximity effects as the “energy dose” diffuses and overlaps with the dose of neighboring spots, giving non-uniform distributions across the arrays with higher levels near the array centers than in the edges and corners.